

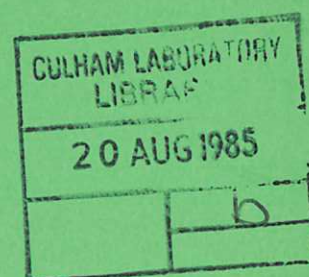


UKAEA

Preprint

ANALYSIS OF INTERNAL MAGNETIC
FLUCTUATIONS IN THE HBTXIA
REVERSED FIELD PINCH

D. BROTHERTON-RATCLIFFE
C. G. GIMBLETT
I. H. HUTCHINSON



CULHAM LABORATORY
Abingdon Oxfordshire

1985

This document is intended for publication in a journal or at a conference and is made available on the understanding that extracts or references will not be published prior to publication of the original, without the consent of the authors.

Enquiries about copyright and reproduction should be addressed to the Librarian, UKAEA, Culham Laboratory, Abingdon, Oxon. OX14 3DB, England.

ANALYSIS OF INTERNAL MAGNETIC FLUCTUATIONS IN THE HBTX1A REVERSED FIELD PINCH

D.Brotherton-Ratcliffe⁺, C.G.Gimblett, I.H.Hutchinson*

Culham Laboratory, Abingdon, Oxfordshire, U.K.

(Euratom/UKAEA Fusion Association)

ABSTRACT

An insertable magnetic probe has been used to investigate the internal structure of the magnetic fluctuations in the HBTX1A Reversed Field Pinch. A statistical method for determining the radial amplitude distributions of instabilities is discussed in some detail. This is used to analyse the experimental data from which it is possible to distinguish three types of instability: At low frequencies (4-20kHz) the dominant internal fluctuations are to be associated with a band of global $m = 1$, $|n| \approx 8$ resistive modes resonant inside the reversal surface. Although non-linear processes are taking place, these modes possess a radial structure in agreement with that predicted by a linear tearing mode stability analysis of the measured equilibrium. At similar amplitudes to these modes there is a short correlation length component ($\lambda_r \approx 3$ cm) which is peaked in the central regions of the discharge. At high frequencies (> 30 kHz) this local activity dominates over the global fluctuations. Finally, at about $1/4$ the peak power of the dominant global instabilities and with a similar frequency dependence, an $m=1$ mode with some ideal MHD characteristics is observed. Stability calculations show that ideal modes whose growth rates are controlled by a resistive wall could have similar radial structure and timescales as this mode.

(Submitted for publication in Plasma Physics and Controlled Fusion)

⁺ Royal Holloway College, London University, UK.

* Nuclear Engineering Department, MIT, Cambridge, Ma 02139, USA.

In the Reversed Field Pinch (RFP)[1] it is thought that fluctuations play an important role in the development and sustainment of a reversed field configuration and that they may also be responsible for the anomalous confinement observed in these devices. Detailed studies of fluctuations thus offer a way to the understanding of the physics of these two important topics, field reversal and transport.

Recently fluctuations have been studied in various machines, notably OHTE [2]; ETA-BETA-II [3], ZT-40(M) [4] and HBTX1A [5,6]. These investigations, while producing new results, also substantiate older measurements from ZETA [7,8] and MkIV torus [9]. From these studies it appears that the principal fluctuations are characterised by an ' $m = 1$ ' symmetry. This is also the case for fast-programmed pinches such as HBTX1 [10]. For HBTX1A, it has been shown that the $m = 1$ modes are to be associated with $|n| = 8$ and are resonant inside the reversal surface.

In this paper a statistical analysis method is developed for distinguishing linearly independent processes from quasi-random data. This is used to analyse measurements from an insertable magnetic probe on HBTX1A. The technique allows, to a large extent, the determination of the radial structures of the various instabilities responsible for the observed (temporally incoherent) fluctuations. The results of this study are compared with predictions from the linear MHD theory applied to the measured magnetic equilibrium.

The magnetic probe is illustrated in figure 1. There are twenty-seven coils divided into nine sets of three. Each set of three comprises a radial, toroidal and poloidal coil, thus defining the time varying magnetic

field in nine equally spaced radial locations. The coils are set into a PTFE former which itself fits into a silica glass sheath, 6mm in (outside) diameter. The entire probe is attached to a bellows assembly which enables the tip of the probe to be positioned anywhere across a minor radius. Typically we operate with the probe extended fully to the minor axis.

Throughout this study we will consider only decaying current discharges of around 100 kA and of about 2 ms duration. The properties of these discharges are little affected by probe insertion [11] and the fluctuation structure as measured by edge coils is the same as that for higher current sustained discharges which have been studied previously [5]. The evolution of the main parameters for a typical discharge is shown in figure 2.

3 DETERMINATION OF THE RADIAL STRUCTURE OF INSTABILITIES

An insertable magnetic probe provides information on the time-history of the magnetic field at a finite number of radial locations. When there is just one mode present, this information can easily be translated into the radial amplitude distribution of that mode. For instance, this may be accomplished by taking the square-root of the radial power distribution. However, when there is more than one mode present the problem of determining the various radial amplitude distributions becomes non-trivial. Since this case typifies the RFP it is of considerable importance to formulate algorithms capable of solving this problem to some extent. In this section we will thus develop an effective solution which will then be used extensively in interpreting probe data in the following sections.

3.1 Introduction To Correlation Matrix Fitting (CMF)

To a certain approximation the fluctuating magnetic field may be regarded as the sum of several (linearly) independent gaussian processes of

zero mean. In such a case the first order statistical moments completely define the combined probability distribution function and hence the correlation matrix, defined as:

$$R_{ij} = \frac{1}{T} \left\langle \int_0^T b_i(t) b_j(t) dt \right\rangle, \quad - (1).$$

represents the totality of information obtainable from the probe data (in a given frequency band). In this definition $b_i(t)$ is the fluctuating magnetic field at the radial position dictated by the suffix i . The integral is a time integral and should be taken over a statistically stationary [12] region of the time history described by the region $\{0, T\}$. Triangular brackets indicate an ensemble average over many statistically similar shots.

The approach we take is thus to assume a finite number of linearly independent or randomly phased processes (global or local modes) and then to use the correlation matrix to define the various radial amplitude distributions characteristic of each process. In this way we sacrifice information about the time variation to gain more information concerning radial structure.

3.2 2-Process CMF Model

To begin with we will assume that the fluctuating magnetic field may be decomposed into just two components; a global mode with a radial correlation length of the order of the minor radius and a local component defined in terms of the correlation matrix:

$$R_{ij} \propto \delta_{ij} \approx \begin{cases} 1 & i = j \\ 0 & i \neq j. \end{cases} \quad - (2)$$

We denote the time dependence of the local contribution by $l_i(t)$ and that of the global contribution by $g_i(t)$. Then, further assuming that there is no radial propagation associated with the global mode, by using equation 1 we

may calculate the correlation matrix:

$$\begin{aligned}
 R_{ij} &= \frac{1}{T} \left\langle \int_0^T (\ell_i(t) + g_i(t))(\ell_j(t) + g_j(t)) dt \right\rangle \\
 &= \frac{1}{T} \left\langle \int_0^T \ell_i(t) g_j(t) dt \right\rangle \quad \text{-(i)} \\
 &\quad + \frac{1}{T} \left\langle \int_0^T \ell_i(t) \ell_j(t) dt \right\rangle \quad \text{-(ii)} \\
 &\quad + \frac{1}{T} \left\langle \int_0^T g_i(t) g_j(t) dt \right\rangle \quad \text{-(iii)} \\
 &\quad + \frac{1}{T} \left\langle \int_0^T g_i(t) \ell_j(t) dt \right\rangle \quad \text{-(iv)}. \quad \text{-(3)}
 \end{aligned}$$

Terms (i) and (iv) vanish since we assume that the local turbulence is not linearly correlated to the global instability (this essentially defines what we mean by linearly independent). Term (ii) will also vanish when $i \neq j$ since this was our definition of local 'turbulence'. Hence we may rewrite equation 3 as follows:

$$\begin{aligned}
 R_{ij} &= \frac{1}{T} \left\langle \int_0^T \ell_i(t) \ell_j(t) dt + \int_0^T g_i(t) g_j(t) dt \right\rangle \\
 &= \bar{\ell}_i \bar{\ell}_j \delta_{ij} + \bar{g}_i \bar{g}_j, \quad \text{-(4)}
 \end{aligned}$$

where the operator ' $\bar{}$ ' denotes a signed root-mean square over the interval $(0, T)$, the sign depending on whether g_i and g_j are in or out of phase. Given the measured correlation matrix this equation may now be solved for the \bar{g}_i by minimisation of the quantity:

$$Q = \sum_i \sum_j (R_{ij} - \bar{g}_i \bar{g}_j)^2, \quad \text{-(5)}$$

which is essentially a non-linear optimisation problem and may be solved numerically by the method of steepest descents [eg 13]. Denoting the n^{th} successive estimate of \bar{g}_i by $\bar{g}_i^{(n)}$ we use the following algorithm:

$$\bar{g}_i^{(n+1)} = \bar{g}_i^{(n)} + \beta \frac{\partial Q}{\partial \bar{g}_i}$$

where
$$\frac{\partial Q}{\partial \bar{g}_i} = -4 \sum_{j \neq i} \bar{g}_j (R_{ij} - \bar{g}_i \bar{g}_j) \quad - (6)$$

and β is a small positive constant. If desired this procedure can be much improved for speed by the use of conjugate gradients [13]. However we find that with LSI 11/23 computers and $N \leq 10$ this is unnecessary. Note that when the \bar{g}_i 's are known, the profile of local turbulence may easily be calculated:

$$\bar{l}_i = \sqrt{\{ R_{ii} - \bar{g}_i \bar{g}_i \}}. \quad - (7)$$

This follows directly from equation 4.

In the above model we have made several very particular assumptions. Notably that the fluctuation activity is due only to two components: a global instability and a local contribution. In equation 5, where we eliminate the local turbulence by not summing with $i=j$, we are thus fitting the correlation matrix with an N -parameter family. However the correlation matrix itself (ignoring diagonals) is a function of $N(N-1)/2$ independent parameters. Hence the value of Q is a strong indication of whether or not the initial assumptions were correct. In fact a better indication is furnished by a chi-squared parameter:

$$\chi^2/N = \frac{1}{N(N-1)} \sum_{i \neq j} \{ R_{ij} - \bar{g}_i \bar{g}_j \}^2 / \sigma_{ij}^2, \quad - (8)$$

where σ_{ij} is the error bar associated with the measured R_{ij} . If χ^2/N is approximately unity then the fit is good and we will have confidence in the initial assumptions. If, on the other hand, χ^2/N is much greater than one, the fit is not consistent with errors and we must adopt another model.

3.3 Many Process CMF Model

The fact that Q depends on many more variables than the number of signals, N , allows us to consider more complicated cases than that of just one global mode and local turbulence. In fact we may generalise our model to the case of there being p linearly independent global modes present in addition to the local turbulence. Extending our previous notation, we denote the time history of the global mode, i by $^i\bar{g}_j$, where j , as usual, indicates radial position. Then in the same fashion as we derived equation 4 we may write:

$$R_{ij} = \bar{l}_i \bar{l}_j \delta_{ij} + \sum_{s=1}^p (s\bar{g}_i s\bar{g}_j) , \quad - (9)$$

where quadratic terms involving different modes cancel due to the linear independence of each global mode. Again we may now solve this equation for the $s\bar{g}_i$'s by the minimisation of a modified Q function:

$$Q = \sum_{i \neq j} \sum (R_{ij} - \sum_{s=1}^p (s\bar{g}_i s\bar{g}_j))^2 , \quad - (10)$$

which leads to a similar algorithm as that in equation 6. At this point we must be careful, however, as equation 10 is invariant under rotations in the function space comprised from the vectors $s\bar{g}$. This can be seen simply for $p = 2$ by noticing that the following transformation leaves Q unchanged:

$$\begin{aligned} ^1\bar{g}_i &\rightarrow (\sin\alpha) \cdot ^1\bar{g}_i + (\cos\alpha) \cdot ^2\bar{g}_i \\ ^2\bar{g}_i &\rightarrow (\cos\alpha) \cdot ^1\bar{g}_i - (\sin\alpha) \cdot ^2\bar{g}_i , \end{aligned} \quad - (11)$$

α being a constant in the interval $\{0, 2\pi\}$. Thus for $p > 1$ the solution of the equations $\partial Q / \partial s\bar{g}_i = 0$ is not unique. Rather the minimum Q is mapped out by the surface of a hypersphere in the p -dimensional $s\bar{g}$ function space.

Hence, to completely determine the global modes of a system we must supply extra information. If we visualise p global modes we will need

$p(p-1)/2$ constraints. Compared with pN , the total number of independent variables that we ultimately wish to know, this number is rather small.

In the many-process CMF model the procedure that we will use in this paper is thus to perform the minimisation of equation 10 in the fashion of equation 6 and then to 'rotate' the resulting modes (e.g according to equation 11) until they satisfy additional constraints.

3.4 Concluding Remarks on CMF

In the light of the non-uniqueness of the many process CMF model it is pertinent to discuss under what circumstances we are justified in using the unique 2-process CMF model. To facilitate this it is advantageous to consider a variant of the many process CMF definition for Q given in equation 10 in which diagonal summation is included. When N is large this would be expected to make little difference to any results that we may deduce and has the merit of making the analysis easier. In this case, under the stipulation that the various global modes are mutually orthogonal in space, the equations $\partial Q / \partial \bar{s} g_i = 0$ can be shown to possess a unique solution in which each global mode is an eigenvector of the symmetric matrix R_{ij} . All other solutions on the general hyperspherical surface in function space can then be generated from this unique set by rotation.

If we now consider a case in which an R_{ij} matrix is constructed from several spatially non-orthogonal global modes and we attempt to recover one of these modes by doing a CMF fit with $p=1$ then the predicted mode will clearly be the largest eigenvector of R_{ij} . There are two cases in which this answer is generally useful. The first is when it is known beforehand that all the global modes of a system are mutually orthogonal in space in which case the largest eigenvector of R_{ij} is the largest global mode. The second case is when it is known or can be inferred that the amplitude of the global modes form a descending series so that the first mode is much larger than

the second and so forth. In this case the largest eigenvector of R_{ij} is, to a good approximation, the largest global mode.

Regarding the many-process CMF model, it is very interesting to note that if mutual spatial orthogonality between global modes can be assumed, then the technique actually specifies all global modes uniquely. In this paper we will not be able to make such an assumption though clearly other future applications may be able to.

4 RESULTS

4.1 Time History Analysis

The most obvious rudimentary way of analysing probe data is to look for similarities in the individual time histories pertaining to a single shot. Figure 3 shows an example of this technique for the B_θ signals obtained from our probe in the frequency range 4-20 kHz. It can be seen from this diagram that there is no unique relationship between the various signals at different radial locations. Rather, on close inspection, it is apparent that many features appearing on one trace do not seem to relate to features on the other traces. Some features, however, can be related and for these it is apparent that maxima on traces of large radial position seem to be associated with minima on traces of small radial position. This is shown more clearly in figure 4 where a least squares linear fit has been computed for each time-step and plotted in a 3-D format. By doing this, features peculiar only to one trace are heavily damped whereas the global traits are accentuated.

We find, then, that many of the features visible on the individual time-histories of the probe data are peculiar to just one coil. These are then local fluctuations. In addition to this, however, we also see the presence of common features to all traces, which represent global

fluctuations. For B_θ these global fluctuations are characterised by the outer and inner regions of the discharge being 180° out of phase. The null point of this 'flipping' motion is about 10 cm. With a similar analysis B_ϕ is found to behave in the same fashion but with a null point near the reversal surface. The B_r component, on the other hand, seems to be in phase throughout the discharge radius. The absolute magnitude of the combined fluctuations is typically about 2 to 3% of the spatially averaged equilibrium field at low frequencies and falls off inversely with increasing frequency as $1/\nu$.

4.2 Radial Propagation And Perturbation Phasing

To gain more information about the character of both these local and global fluctuations we must resort to a statistical analysis. An important question concerning the fluctuations of a system is the existence of radial propagation. If this occurs, it might produce an energy transport which could explain the anomalous confinement observed in the RFP. In order to investigate propagation effects we define the normalised time-delayed cross correlation matrix as:

$$R_{ij}(\tau) = \frac{\langle \int_0^T b_i(t) b_j(t+\tau) dt \rangle}{\{ \langle \int_0^T b_i^2(t) dt \rangle \}^{1/2} \{ \langle \int_0^T b_j^2(t+\tau) dt \rangle \}^{1/2}} \quad - (12)$$

where $b_i(t)$, as usual, represents the fluctuating magnetic field at the radial location dictated by the suffix i and τ is a time delay parameter. Figure 5 shows an example of this matrix for B_ϕ in the sustainment phase of the discharge, where it is clearly apparent that $R_{ij}(\tau)$ has its greatest value at zero time delay for each i and j . In fact, from an estimation of the associated errors we may calculate that the greatest phase difference between any two coils is at most about $\pi/10$. Exactly similar results are

found to hold for B_r and B_θ and so we may conclude that there is no evidence for global propagation within the statistical accuracy.

In order to investigate the phasing between the various fluctuating field components it is useful to define the phase spectrum between two signals $x(t)$ and $y(t)$:

$$\phi_{xy}(\nu) = \text{Arg} \langle x^*(\nu) y(\nu) \rangle, \quad - (13)$$

which measures the average phase difference, as a function of the frequency ν , between the two signals. '*' denotes complex conjugate. Figure 6 shows the two examples of $\phi(B_\phi, B_\theta)$ and $\phi(B_\phi, B_r)$ computed at $r \approx 14\text{cm}$. Clearly, in the region of 4-20 kHz B_ϕ and B_θ are in phase whereas B_ϕ and B_r are out of phase by about $\pi/2$. At higher frequencies, particularly for $\phi(B_\phi, B_r)$ the phase becomes randomised largely due to a rapid decrease in absolute power. In some discharges $\phi(B_\phi, B_r)$ appears to be a little less than $\pi/2$. However $\phi(B_\phi, B_\theta)$ tends always to remain approximately at zero.

4.3 Radial Structure

Now that we understand some of the basic properties of the magnetic fluctuations, we would like to have a more detailed knowledge of their radial structure. Since we have already discovered from a cursory inspection of the individual time histories that there is more than one process involved we must rely on the CMF analysis model developed in section 3. This model is particularly appropriate as there is no evidence for radial propagation (see above). It is worth noting that it is possible to formulate models which account for propagation but they all suffer from non-uniqueness problems in the predicted radial structures.

4.3.1 2-process CMF Model

As a first approximation we regard the fluctuations as being composed of two linearly independent processes, a global and local component. From the results so far this would represent our best guess at the simplest possible structure. With this approximation we could use the zero-time delay correlation matrix defined in equation 1 to choose the most likely radial distributions of the local and global modes by using the iterative algorithm outlined in equation 6. As it turns out, however, it is better to use a quasi-normalised version of the correlation matrix defined as:

$$R_{ij} = \left\langle \frac{\frac{1}{T} \int_0^T b_i(t) b_j(t) dt}{\frac{1}{N} \sum_{k=1}^N \left\{ \int_0^T b_k^2(t) dt \right\}} \right\rangle, \quad - (14)$$

but otherwise to proceed as outlined above. The reason for adopting this strategy is that for each discharge the fluctuation structure appears to remain roughly the same but with widely varying amplitudes. Hence, if we were to use the definition given in equation 1, the error bars which we would calculate, a standard error in the mean over many shots, would be largely linearly dependent. By using this quasi-normalised form what we are essentially doing is restricting errors so that they pertain to the structure of the fluctuations and not to the absolute amplitude. Using this method we are able to predict accurate relative amplitude distributions for the assumed component processes. These may then be translated into absolute estimates by means of multiplication by a spatially averaged fluctuation amplitude.

Figure 7 shows the measured correlation matrix for B_ϕ taken for twelve shots in the frequency band 4-20 kHz. Also shown in this diagram is the computed correlation matrix representing the best fit. It is clear that the fit is quite good on all off-diagonal components. In fact the chi-squared

parameter defined in equation 8 has a value of about 2.5 and so we may express confidence in our initial assumptions. Figure 8 shows the predicted global-mode radial amplitude distribution for this fit and also for B_θ and B_r obtained from similar fits. Now, in principle, the local turbulence profile is defined by the mismatch between the measured and fitted correlations (e.g. equation 7). However it would be a mistake to interpret all the mismatch on diagonal elements in figure 7 as being due to local turbulence. In particular we will see that by assuming more than one global process it is possible to obtain better diagonal fits. At this point we should also mention that there are problems associated with the fact that the probe extends to the geometrical minor axis rather than the plasma axis, which is 3 cm shifted due to toroidal equilibrium [14]. This essentially means that the central B_r coil actually measures B_θ and vice-versa. However, it turns out that these effects largely cancel for the global modes due to their 'm = 1' symmetry and the fact that B_r is temporally $\pi/2$ out of phase with B_θ .

So far we have been able to elucidate the relative radial structure of the three field components of the dominant global instabilities. However, since we have calculated these structures separately, we cannot be sure that they are all associated. For instance, suppose there were actually several global modes present in the plasma, of which the dominant instability had virtually no field component in one direction. In such a case our algorithm would choose, for this field component, the next most dominant mode. And so we would obtain a set of three radial amplitude distributions which were not all associated. To confirm that our above radial estimates, given in figure 8, are in fact associated we can fit the cross-component correlation matrix. For instance, to obtain the associated radial structures for B_ϕ and B_θ we simply minimise:

$$Q = \sum_{i \neq j} \{ R_{ij}^{\theta\phi} - \bar{g}_{\theta i} \bar{g}_{\phi j} \}^2, \quad - (15)$$

where $\bar{g}_{\theta i}$ and $\bar{g}_{\phi i}$ are the θ and ϕ -components of the global radial amplitude vector and $R_{ij}^{\theta\phi}$ is the quasi-normalised theta-phi cross-component correlation matrix defined as:

$$R_{ij}^{\theta\phi} = \frac{\frac{1}{T} \int_0^T b_{\theta i}(t) b_{\phi j}(t) dt}{\frac{1}{N} \left\{ \sum_{k=1}^N \int_0^T b_{\theta k}^2(t) dt \right\}^{1/2} \left\{ \sum_{k=1}^N \int_0^T b_{\phi k}^2(t) dt \right\}^{1/2}} \quad .-(16)$$

Fitting this matrix we obtain radial variations for B_θ and B_ϕ fairly similar to those in figure 8 which confirms that the θ and ϕ radial amplitudes of figure 8 are to be associated with the same mode. In addition fitting $R^{\theta\phi}$ establishes the relative phasings between B_θ and B_ϕ . Specifically, B_θ is found to be in (temporal) antiphase with B_ϕ in both the inner and outer regions of the discharge but is in phase in the central region. This agrees well with phase spectral estimates similar to those mentioned above.

It is worth noting that the cross-component matrix contains twice as much information as the auto-component matrix since it is not symmetric. This allowed us in equation 15 to fit twice as many parameters as usual but with the same accuracy. One could thus envisage the possibility of using both auto and cross matrices to predict all three field components by minimising a combined Q function defined as:

$$Q = \sum_{i \neq j} \left\{ \alpha [R_{ij}^{\theta\theta} - \bar{g}_{\theta i} \bar{g}_{\theta j}]^2 + \beta [R_{ij}^{\phi\phi} - \bar{g}_{\phi i} \bar{g}_{\phi j}]^2 \right. \\ + \gamma [R_{ij}^{rr} - \bar{g}_{r i} \bar{g}_{r j}]^2 + \delta [R_{ij}^{\theta\phi} - \bar{g}_{\theta i} \bar{g}_{\phi j}]^2 \\ \left. + \epsilon [R_{ij}^{\theta r} - \bar{g}_{\theta i} \bar{g}_{r j}]^2 + \zeta [R_{ij}^{\phi r} - \bar{g}_{\phi i} \bar{g}_{r j}]^2 \right\}, \quad .-(17)$$

where the constants α to ζ should be suitably chosen so as to weight the fit to each correlation matrix according to its statistical errors. In principle this would be expected to allow us to estimate the amplitude vector associated with a given mode with greater accuracy. Further, this

method defines the relative phasings between the field components and of course there is no association problem. However there is one problem in that we already know that B_r is about $\pi/2$ out of phase with B_θ and B_ϕ and so $R_{ij}^{\theta r}$ and $R_{ij}^{\phi r}$ are by definition very small (and hence prone to large errors). This can be resolved by forming a new $B_r(t)$ time-history by taking the Fourier transform of the initial $B_r(t)$, shifting the phase by $\pi/2$ and then inverse Fourier transforming. By renormalising the resultant radial amplitudes we are then able to plot our best possible estimate of the amplitude vector associated with the dominant global instability. This is shown in figure 9.

There are a number of points we may extract from this graph. Firstly the B_ϕ trace appears to almost intersect the minor axis with a non-zero gradient. Secondly we see that on axis $\tilde{B}_r = -\tilde{B}_\theta$. By considering the single valuedness of the fields at the origin in a cylindrical geometry this may be shown to imply that the process is at least partially $m = 1$. Assuming only $m = 1$, the observation that $\tilde{B}_\phi \approx -2\tilde{B}_\theta$ at the wall allows us calculate an $|n|$ -number of (very) approximately six from the equation $\nabla \times \tilde{\mathbf{B}} = 0$. Finally, from the fact that \tilde{B}_r does not cross zero at any point in the discharge radius we may identify the mode as being resistive.

In order to relate this picture to other measurements we may use arrays of edge coils to calculate the poloidal and toroidal mode spectra [5,6]. Figure 10 shows these spectra plotted for both B_θ and B_ϕ . The dominant feature on the n -spectrum is a band of instabilities centred around $|n| = 8$. The m -spectrum shows dominantly $m = 1$. By forming the 'association spectrum' [5], we may link these two features and show that the most powerful instabilities are a band of resistive $m = 1$ modes of $|n| \approx 8$ resonant inside the reversal surface. In addition to this, however, there also appears to be some $m = 0$ on B_ϕ and some $m = 2$ and low n -number features on B_θ . Virtually all the $m = 2$ may be explained by linear coupling due to toroidicity [5]. The low n -number features on B_θ can be shown to be

indicative either of $m=0$, $n=0$ modes or low n , $m = 1$ modes.

So the edge coil measurements are in good agreement with the CMF model predictions for the dominant global instability. However, as we have seen, the edge coils also predict other modes of lower power, the most obvious of which are the $m = 0$.

4.3.2 3-process CMF Model

By assuming a two-process fit we have seen that it is possible to obtain fits to the various correlation matrices with a chi-squared parameter of about three. There is thus information to be gained by including another process. Indeed, as we have discussed above, this may lead to the identification of other modes predicted by the edge-coil data. Therefore we will now assume two linearly independent global processes and a local component. With this type of model, as we discussed in section 3, CMF will not specify the two global modes uniquely but rather it will specify a 1-parameter family of possible radial profiles connected together by the rotation transformation given in equation 11. It should be noted that as long as the particular second global process which is spatially orthogonal to the first is small in amplitude then the rotation family will always contain one mode very similar to our original first global process.

As before we start by fitting the auto-component matrices. Figure 11 shows, for each field-component, that member of the rotation family for which the two component processes are approximately spatially orthogonal and, as an example, figure 12 shows the fit to $R^{\theta\theta}$. All of the autocomponent fits are typically much better now, being characterised by a chi-squared value of about unity.

It is apparent from figure 11 that the first global process obtained with the three-process CMF model is almost exactly the same as our previous results using the two-process model. This is actually not a consequence of

the smaller amplitude of the second global process but is a direct result of the orthogonality criterion we used to select out one member of the B_θ , B_ϕ and B_r rotation families. The reason for employing this criterion is that it minimises the amplitude of the second global process for each field component. Hence figure 11 demonstrates that our experimental measurements require a second global process of a peak amplitude of at least just under half that of the first global process.

A question which now arises is whether this second global process might be explained by phase distortions or a plasma shift phenomenon. In fact one can show that propagation effects, which lead to different phasing of different coils, act to create spurious processes. However, taking the B_ϕ component as an example, if the second process is regarded as a phase distortion of the first, one is led to the belief that there are phase differences of the order of $\pi/2$ between various coils. As we have seen in section 4.2 the phase of B_ϕ is the same on all coils to within about $\pi/10$ and so the second process cannot be explained in terms of a phase distortion. The explanation in terms of an equilibrium plasma shift is again inadequate since excluding the first two coils, which are the ones affected by this shift, does not alter the results. Also a theoretical analysis of the expected effects of such a shift does not explain the observed form of the radial distributions of the second process.

We must conclude that the second global process is a real effect. However, as before, we cannot be sure that each field-component of this process is associated. To find this out we must proceed by the type of prescription outlined in equations 15 and 17, fitting both auto and cross-component correlation matrices. A point to realise here is that, by including cross-component matrices in the minimisation of Q , the number of rotation angles needed to specify the composite rotation family for all field components is reduced from three to one. Without cross-component correlations each field component is unspecified by one rotation angle.

With such correlations the three angles are locked together.

Using the technique referred to above we find that all three components are indeed associated and we may plot one member of the 1-parameter rotation family of the combined renormalised second global process vector. This is shown in figure 13. The criterion used to select this particular member of the rotation set is that of maximum spatial orthogonality between the first and second global process vectors. The fact that the overall shape of figure 13 is very similar to the second global process of figure 12 indicates a high degree of such orthogonality. Another interesting feature of figure 13 is that at $r = 0$ $\tilde{B}_r \approx -\tilde{B}_\theta$ and $\partial\tilde{B}_\phi/\partial r \neq 0$. Since this also approximately holds for the first global process this indicates that the second process, like the first, must be at least partially $m = 1$. To somewhat substantiate this we can recall that the edge coil analysis rules out an $m > 1$ explanation on account of absolute power considerations.

Returning to figure 12, which shows the fit to $R^{\theta\theta}$ we can now use equation 7 to calculate the profile of local turbulence. We must be careful however, since the probe is inserted up to the geometrical minor axis and not to the plasma axis, the two being separated by the Shafranov shift. As we discussed briefly before this means that the first B_θ coil actually measures B_r and vice-versa. Nevertheless it can be shown that the Shafranov shift does not affect the local turbulence profiles for B_θ and B_r deduced from the diagonal element mismatch apart from interchanging the two components on axis. For B_ϕ , the Shafranov shift acts to create a spurious quasi-local process producing anomalous diagonal and next-to-diagonal mismatch on the first two coils. From figure 11 (and from the fits to $R^{\phi\phi}$ and R^{rr} not shown) it is thus apparent that the B_θ local turbulence is peaked on axis, falling, within errors, to zero at the edge of the discharge. For B_ϕ , allowing for the Shafranov shift effect, the local activity seems to peak a few centimetres out from the origin but nevertheless falls, within errors, to zero at the edge of the discharge. For

both B_ϕ and B_θ the peak amplitude of the local turbulence is roughly equal to that of the global modes. For B_r , the local activity is subject to some uncertainty due to a lack of coils at large radial positions. However, evidence suggests that it follows the B_θ behaviour but at a lower amplitude.

4.3.3 Higher Process CMF Models

In principle it is possible to extend our previous analysis to cover three or more global modes using mutual spatial orthogonality to define a unique series. In fact we find that such a series is rapidly descending in amplitude, reaching statistical limits at the third global mode. The conclusion to be drawn from this is that any higher order global modes are either very small in amplitude or are very similar in shape to a linear combination of the first two global modes.

4.3.4 High Frequency And Setting-up/Termination Results

A similar analysis to that discussed above for the sustainment phase of the discharge in the frequency band 4-20 kHz has been applied to the setting-up and termination phases and to higher frequencies. A striking feature which appears is that as the frequency increases the local turbulence becomes dominant over the global instabilities. Indeed, in the range 50-100 kHz the global modes are barely visible. This is shown for B_ϕ in figure 14, where we plot a normalised cross correlation matrix. Fitting these high frequency correlations actually yields very similar global patterns to those we have been discussing above, although the decreasing amplitude means that we may only use the two-process algorithm.

Regarding the setting-up and termination phases of the discharge, our study again reveals the same qualitative picture for the global and local

modes. However there are two effects of interest concerning the local turbulence profile. In the setting-up phase, while the B_ϕ local component remains at the same amplitude in relation to the global component, the B_θ term becomes much stronger. In the termination phase both the B_θ and the B_ϕ components become stronger in relation to the global modes.

5 LINEAR STABILITY OF THE EQUILIBRIUM FIELDS

5.1 Introduction

The derivation of the equilibrium magnetic field profiles from probe data has been reported elsewhere [11]. Here we report results obtained from analysing these profiles for linear stability to ideal current and pressure driven modes and, in the limit of infinite Lundquist number, to tearing modes. The rationale for considering the linear theory, when in reality instabilities are not observed to grow exponentially with time, is that the observed fluctuations are small in comparison to the neighbouring equilibrium and thus the dominant mode-saturation processes might be expected only to be quasilinear. Figure 15 shows the equilibrium field profiles measured directly from the probe. The curves fitted to the measured points are least-squares polynomials. It should be noted that before testing these profiles for stability it is necessary to apply a small correction [11] for the outward Shafranov shift.

5.2 Ideal Stability

A general guide to the stability to ideal pressure driven instabilities is furnished by the Mercier criterion (for stability) [15]:

$$\left\{ \frac{B_\phi^2}{B^2} \right\} \left\{ \frac{r}{q} \frac{dq}{dr} \right\}^2 + 8\mu_0 r \frac{dP}{dr} \frac{(1-q^2)}{B^2} > 0 . \quad - (18)$$

The first term represents the shear of the magnetic field lines and is always stabilising whereas the second term, which depends upon the pressure gradient is, for typical RFP configurations, destabilising. Within the large errors associated with estimating the pressure gradient from the measured fields we find that this criterion is marginally satisfied for all radii.

In order to analyse the ideal linear stability to current driven modes we use the Newcomb procedure [16] applied to deflated field profiles which possess no pressure obtained by calculating the μ profile, defined as $\underline{j} \cdot \underline{B} / B^2$, and then solving the force-free relation $\nabla \times \underline{B} = \mu \underline{B}$ for the fields. In actual computation we find complete stability to all current driven ideal modes when the liner is regarded as an infinitely conducting wall. However, if we disregard the liner and take the shell as being the relevant infinitely conducting wall we find that, within errors, on-axis $m = 1$ current driven modes have marginal stability.

5.3 Resistive Tearing Mode Stability

The method of Δ' analysis [17] offers a very simple solution to investigating the linear stability properties of tearing modes in the limit of infinite Lundquist number. It has been shown that this method agrees well on the prediction of marginal stability points with finite Lundquist number codes as long as $S > 10^3$ [18]. For HBTX1A $S \approx 10^4$ to 10^5 .

The basic element involved in Δ' analysis is to calculate, for given m and n numbers, a parameter Δ' such that if $\Delta' > 0$ there is instability and if $\Delta' < 0$ then there is stability [19,20,21]. In the case of $\Delta' > 0$ the value of Δ' is directly related to the growth rate of the particular mode pertaining to that Δ' . As for ideal current driven instability tests, for self-consistency, we eliminate pressure from the field profiles by the deflation process described above.

Figure 16(a) shows Δ' as a function of the parameter $k_z a$ ($k_z \equiv n/R$ where R is the major radius, and a is the liner minor radius) for poloidal mode number, $m = 0$. In this case the liner has been assumed to be an infinitely conducting wall. Clearly for low k_z , corresponding to $n \leq 2$, there is instability whereas for high k_z there is stability. Similar $m = 0$ stability calculations where a vacuum region is included, the liner conductance assumed negligible and the shell taken as an infinitely conducting wall indicate slightly higher Δ' but otherwise very similar results. The $m = 0$, $|n| = 0$ activity observed by the edge coils (figure 10) would thus seem to be explicable in terms of the linear theory.

The situation for the $m = 1$ instabilities is not quite so simple. Figure 16(b) (trace 1) shows Δ' for $m = 1$ plotted as a function of the resonant radius. As with the $m = 0$ case the infinitely conducting wall has been taken as the liner. It is clear that Δ' certainly peaks at about $r = 0.4a$, where edge coils indicate a dominant instability, but it never actually goes positive. By ignoring the liner conductance and taking the shell as the infinitely conducting wall this picture does not qualitatively change although Δ' does increase. However, by steepening the equilibrium μ -profile to the edge of the estimated errors (figure 17(b)) in a plausible fashion an instability can be generated. This is shown in trace 2 of figure 16(b). Thus the $m = 1$ linear stability appears, within errors, approximately marginal at the helicity observed for the dominant fluctuations.

In order to pursue the question concerning the origin of the observed $m = 1$ modes it is possible, for the 'perturbed' equilibrium μ profile of figure 17(b), to compare the eigenfunctions associated with the consequent instability with the radial amplitude distributions reported in section 4 of this paper. Of course the latter distributions are uncertain to a rotation and so the real global modes will be linear combinations of these distributions. However, since the second global mode of figure 13 is much

smaller than the first global mode all rotations will produce (at least) one global mode fairly similar to our first process. Figure 18 shows the calculated $m = 1$ eigenfunctions. Comparing them with the measured first process shown in figure 9 it is apparent that there is good agreement. It should be noted that calculating the stable eigenfunctions using the non-perturbed μ profile yields very similar results.

Stability calculations for $m \geq 2$ show $\Delta' \ll 0$ indicating complete stability.

6 DISCUSSION

An analysis of the internal structure of magnetic fluctuations obtained from measurements from an insertable magnetic probe has been presented. To distinguish linearly independent processes (modes or sets of modes with similar radial structures) the technique of correlation matrix fitting (CMF) has been developed and applied to the probe data. As a result, in the sustainment phase of the discharge, it has been possible to distinguish three linearly independent processes simultaneously and to obtain information on their radial distributions.

The most prominent process distinguishable at low frequencies (4-20 kHz) possesses a radial structure which identifies it with the global $m = 1$, $|n| \approx 8$ instabilities detected by edge coils. The fact that $\tilde{B}_r \neq 0$ for any $r < r_{\text{wall}}$ substantiates previous timescale arguments [5] suggesting that these modes are resistive. In addition, the agreement of the 'measured' radial amplitude distribution with the field-eigenfunctions of the most unstable tearing mode, computed for the measured equilibrium, demonstrates the close connection with the linear or quasi-linear theory. For non-resonant radii, of course, such agreement is at least partly to be expected as here the form of the resistive MHD field-eigenfunctions simply depends on a small amplitude helical equilibrium.

In this study the stability of resistive pressure driven modes has not been addressed. This is because the pressure profile deducible from probe data is not accurate enough for such a study. Indeed it is very hard to see that further measurements will change this situation. However, it has been shown that the observed $m = 1$ fluctuations can be adequately interpreted in terms of tearing modes of almost marginal stability. Previous measurements indicated that the temporal behaviour of the $m = 1$ modes is that of a quasi-cyclic process [5] with different n -numbers being present at different times. This process would fit in nicely with the observation of marginal stability since the measured equilibrium fields represent an average over many such cycles. However it is not possible to exclude the g -mode as a possible source of the observed $m = 1$ fluctuations.

For the case of the $m = 0$ tearing instability it has been shown that the measured equilibrium is in fact always unstable. Edge coil measurements predict a mode of this type although there is a slight uncertainty about the n -number which might possibly be zero as well. In this case the observed $m = 0$ modes might well be associated with mode-mode coupling effects produced by the $m = 1$. Further investigation will be required to elucidate this.

The second most prominent process discernible corresponds to local fluctuations of a correlation length of about 3 cm. This local turbulence is peaked in the central regions of the discharge at an amplitude similar to the dominant global modes and falling, within errors, to zero at the plasma edge. At high frequencies (>30 kHz) these fluctuations dominate over the global modes.

Observation of such local modes has been reported before, notably in ZETA [22] and more recently in ETA-BETA-II [3]. In all cases these observations have been confined to high frequencies where the global instabilities are less apparent. The importance of the observations reported here is that, even at low frequencies, local fluctuations are of a

comparable importance to that of the larger scale lengths.

The final process discernible is a global mode of a peak amplitude of at least about 1/2 that of the dominant first process and possessing a similar frequency dependence. The actual radial profile of this mode is undefined to within a linear combination with the first global process shown in figure 9. To define the coefficient of this linear combination or 'rotation' and thus to expose the true second process eigenfunction we must use some external constraint. Without such a constraint, however, it is still possible to deduce a significant $m = 1$ nature for this process as the form of both the first and second global processes is the same at the origin.

Now as we have seen from the ideal stability analysis, within errors, the measured equilibrium is marginally unstable to on-axis current driven modes if we ignore the stabilising effect of the liner. However, by inspection of the measured equilibrium q-profile (figure 19) we see that the nearest integral mode number to the axis is actually $|n| = 6$ which is resonant at $r = 8$ cm. Thus, taking into account the toroidal nature of the HBTX1A pinch, we must conclude that the most unstable ideal mode will have $|n| = 6$. Within errors this mode still plausibly has marginal instability given the intrinsic error in the minor radial position of the shell in a Shafranov-shifted plasma.

The timescales observed for the third process are clearly not consistent with direct ideal instability. However we have seen that if the liner is taken as the relevant infinitely conducting wall then there is no instability. The fact that the liner is resistive means that instability can occur [23] but at a timescale determined by field diffusion through the liner. At low frequencies this timescale may be estimated by matching the value of $(1/\tilde{B}_r)d\tilde{B}_r/dr$ at the liner as computed by (i) the integration of the linearised forms of $\nabla \times (\underline{J} \times \underline{B}) = 0$ and $\nabla \cdot \underline{B} = 0$ from the resonance to the liner and (ii) by the solution of Laplace's equation in the vacuum region between the

liner and shell. Doing this we find $\omega \leq 50\text{kHz}$, comparable with our observations. Further to this, if we assume that this timescale is much smaller than that of resistive diffusion, a small layer expansion about the resonance shows that the amplitude of the mode (magnetic field) eigenfunction is very small from the origin to the resonance. This provides a good test as to whether the 3rd process is really a low frequency ideal mode as it constitutes many more constraints than we could hope to fit using the available one parameter rotation. In practice we find that by applying the rotation transformation of equation 11 to the first and second global modes, at one unique value of α (or equivalently at one rotation angle), within statistical errors, $\tilde{B}_r = \tilde{B}_\theta = \tilde{B}_\phi \approx 0$ from $r = 0$ to $r \approx 6$ cm for the second global process. This is shown in figure 20. Discrepancies might be explained by the fact that the instability time is not much faster than the tearing growth time, making a sheet current approximation invalid. The first global process is, as expected, largely unaffected. We would thus conclude that the 3rd process could be explained in terms of a 'liner-liberated' current driven ideal instability.

Since the ideal stability is, within errors, marginal it should be mentioned that there exists another explanation for the observed timescales of the third process. It has been shown [23] that for the near-marginal case hybrid growth rates can be obtained for a resistive wall. Thus if we consider the shell to be resistive and further that the marginal point for stability is just on the shell then we might expect 'resistive-shell' hybrid timescales. These timescales would, of course, be modified by the resistive liner. Owing to the critical dependence on the condition of marginal stability we are unable to estimate exact growth rates. However we cannot rule out this shell-hybrid explanation.

Finally we come to the question of radial propagation. Within errors we find that there is no such propagation and hence there is no evidence that energy is directly carried out of the plasma by this mechanism. The

observation that there exists an almost $\pi/2$ phase shift between B_r and B_θ (or B_ϕ) is indicative of propagation in the toroidal or poloidal directions (consider $\nabla \cdot \underline{B} = 0$). This supports previous observations of plasma rotation [5,6].

The present study has provided some interesting and important results. Nevertheless there are still many unanswered questions which need attention. At least some of these areas may be capable of being studied by a more precise but otherwise similar type of analysis than we have used here. In particular the CMF analysis model may be used to study many more global instabilities given better accuracy and more simultaneous measurements of the fluctuating field at different radial positions. This may shed light on aspects such as the non-linear couplings present between modes and exactly what they are. The local fluctuations present a little more of a problem and in general these may require different experimental techniques to learn about their detailed structure and behaviour.

7 CONCLUSIONS

In this paper we have discussed results obtained from an insertable magnetic probe on the RFP HBTX1A concerning the internal structure of the magnetic fluctuations. A statistical technique has been developed for the determination of the radial amplitude distributions of instabilities. This has been applied to the probe data where it has been possible, in the sustainment phase of the discharge, to distinguish three types of instability. At low frequencies (4-20 kHz) the dominant internal fluctuations are a band of global $m = 1$ $|n| \approx 8$ resistive modes. The radial structure of these modes is in good agreement with that predicted by a linear tearing mode stability analysis of the measured equilibrium. Of similar amplitudes to these modes there is also a short correlation

component (correlation length $\lambda_r \approx 3\text{cm}$) which is peaked in the central regions of the discharge. At high frequencies this local turbulence dominates over the global modes. Finally at about $1/4$ the peak power of the dominant global modes and with a similar frequency dependence, an $m = 1$ mode with some ideal characteristics is observed. Stability calculations show that ideal modes of $m = 1$, $|n| = 6$ whose growth rates are controlled by a resistive wall could have similar radial structure and timescales as this mode. No evidence is found for radial propagation but phasing of the fluctuating field indicates that toroidal and poloidal propagation occur. The internal structure of fluctuations in the termination and setting-up phases have been studied. Results indicate a similar scenario to the sustainment phase but poorer statistics do not allow the clear observation of the $m = 1$, $|n| \approx 6$ mode.

8 ACKNOWLEDGEMENTS

The authors would like to thank M.K.Bevir, R.J.Hastie, J.B.Taylor, H.A.B.Bodin, M.Malacarne and M.G.Rusbridge for fruitful discussions.

REFERENCES

- /1/ Bodin H A B and Newton A A: Nucl. Fusion 20 1255 (1980).
- /2/ e.g. La Haye R J et al: General Atomic Report GA-A16945 (1982).
- /3/ Antoni V, Ortolani S: Plasma Phys. 25 799 (1983).
- /4/ e.g. Watt R G, Nebel R A: Phys. Fluids 26 1168 (1983).
- /5/ Hutchinson I H, Malacarne M, Noonan P, Brotherton-Ratcliffe D: Nucl. Fusion 24 59 (1984).
- /6/ Malacarne M, Hutchinson I H, Brotherton-Ratcliffe D: Proc. Varenna Conf. Italy (1983).
- /7/ Rusbridge M G, Lees D J, Saunders P A H: Nucl. Fusion Suppl. Part 3 895 (1962).
- /8/ Robinson D C, Rusbridge M G, Saunders P A H: Plasma Physics 10 1005 (1968).
- /9/ Rusbridge M G, Jones H W, Lees D J, Saunders P A H, Witalis E A: J. Nucl. Energy Part C: Plasma Physics 3 98 (1961).
- /10/ Verhage A J L, Furzer A S, Robinson D C: Nucl. Fusion 18 457 (1978).
- /11/ Brotherton-Ratcliffe D, Hutchinson I H: Culham Report CLMR246 (1984).
- /12/ Bendat J S and Piersol A G: 'Random Data: Analysis and Measurement Procedures' Wiley-Interscience (1980).
- /13/ 'Handbook of Applicable Mathematics' Ed Ledermann W, Churchhouse F Volume III Chapter 11 Wiley (1981).
- /14/ Shafranov V D in Reviews of Plasma Physics 2 p130 Ed Leontovich M A Consultants Bureau New York.
- /15/ e.g. Bateman G: 'MHD Instabilities' p67 (MIT, Cambridge, Mass.) (1978).
- /16/ Newcomb W A: Ann. Phys. (N.Y.) 10 232 (1960).
- /17/ Furth H P, Rutherford P H, Selberg H: Phys. Fluids 16 1054 (1973).
- /18/ Robinson D C et al: Culham Report CLMP710 and submitted to Reports on Progress in Physics (1983).
- /19/ Furth H P, Killeen J, Rosenbluth M N: Phys. Fluids 6 459 (1963).
- /20/ Johnson J L, Greene J M, Coppi B: Phys. Fluids 6 1169 (1963).
- /21/ Coppi B, Greene J M, Johnson J L: Nucl. Fusion 6 101 (1966).
- /22/ Goedbloed et al: Nucl. Fusion 12 649 (1972).
- /23/ Robinson D C: Culham Report CLM-R199 (1979).

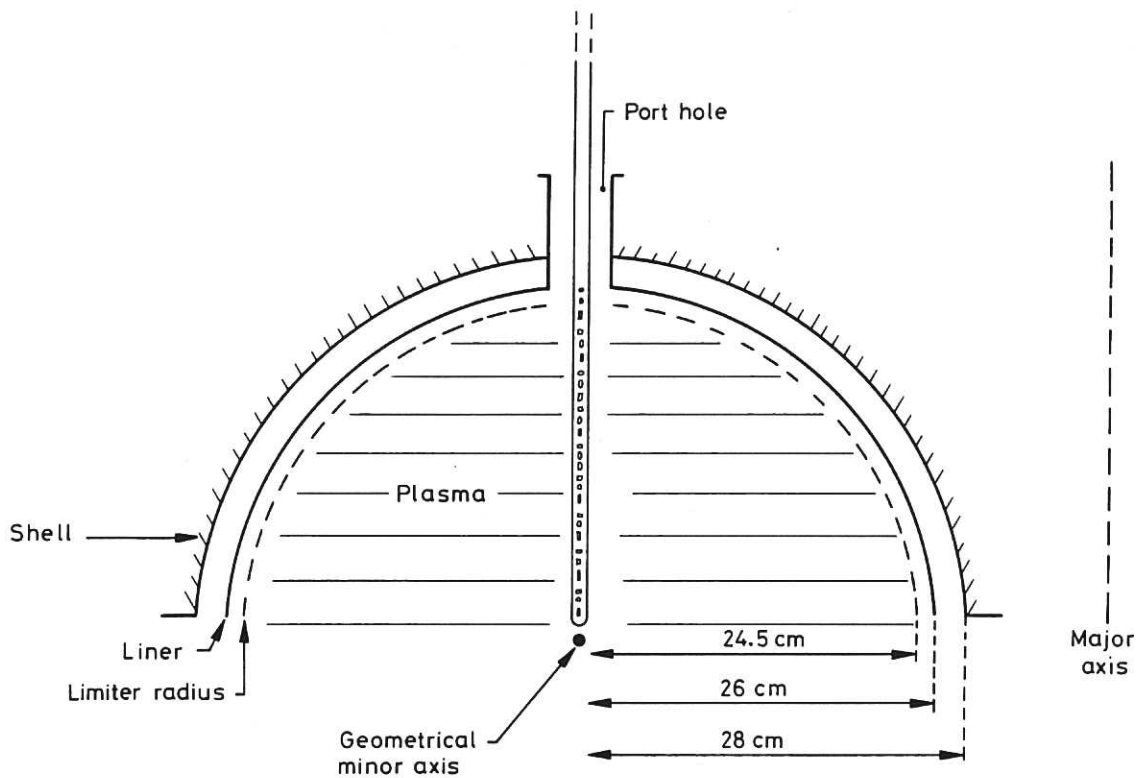


Fig.1 Schematic illustration of the insertable magnetic probe.

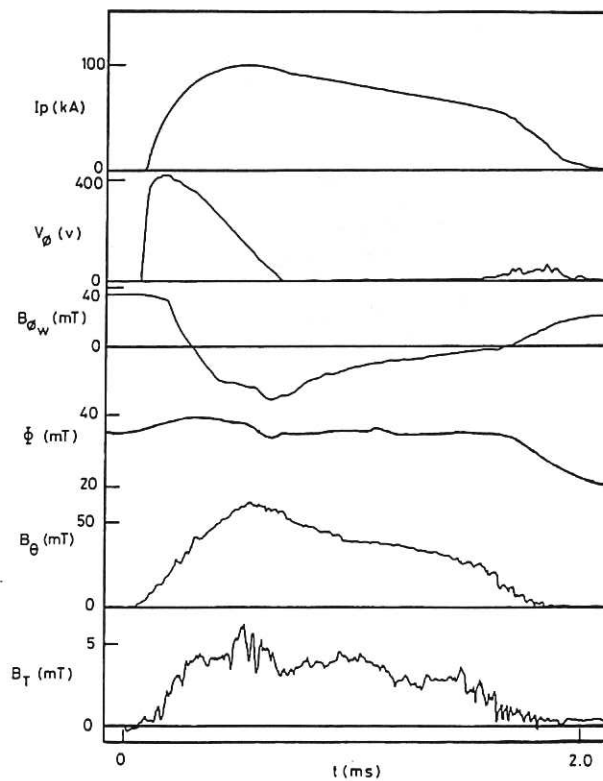


Fig.2 Typical parameter traces for the discharges considered: toroidal current (I_p), loop voltage (V_ϕ), toroidal field at the wall ($B_{\phi w}$), toroidal flux (Φ), typical B_θ probe trace (B_θ^P) and typical B_r probe trace (B_r^P).



Fig. 3 Filtered time histories (frequency band 4—20kHz) for $7B_\theta$ probe traces.

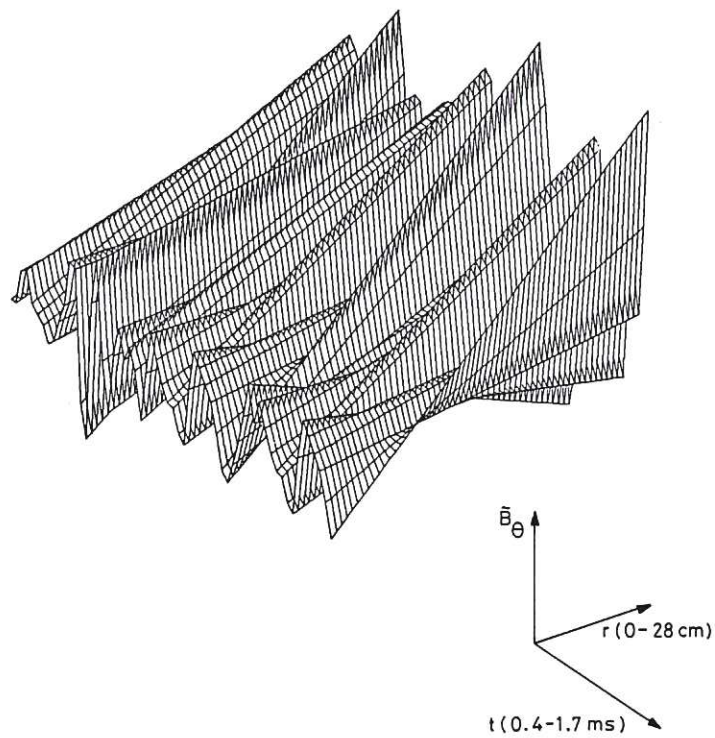


Fig. 4 Linear profile fit to Fig.3 showing 'flipping' motion.

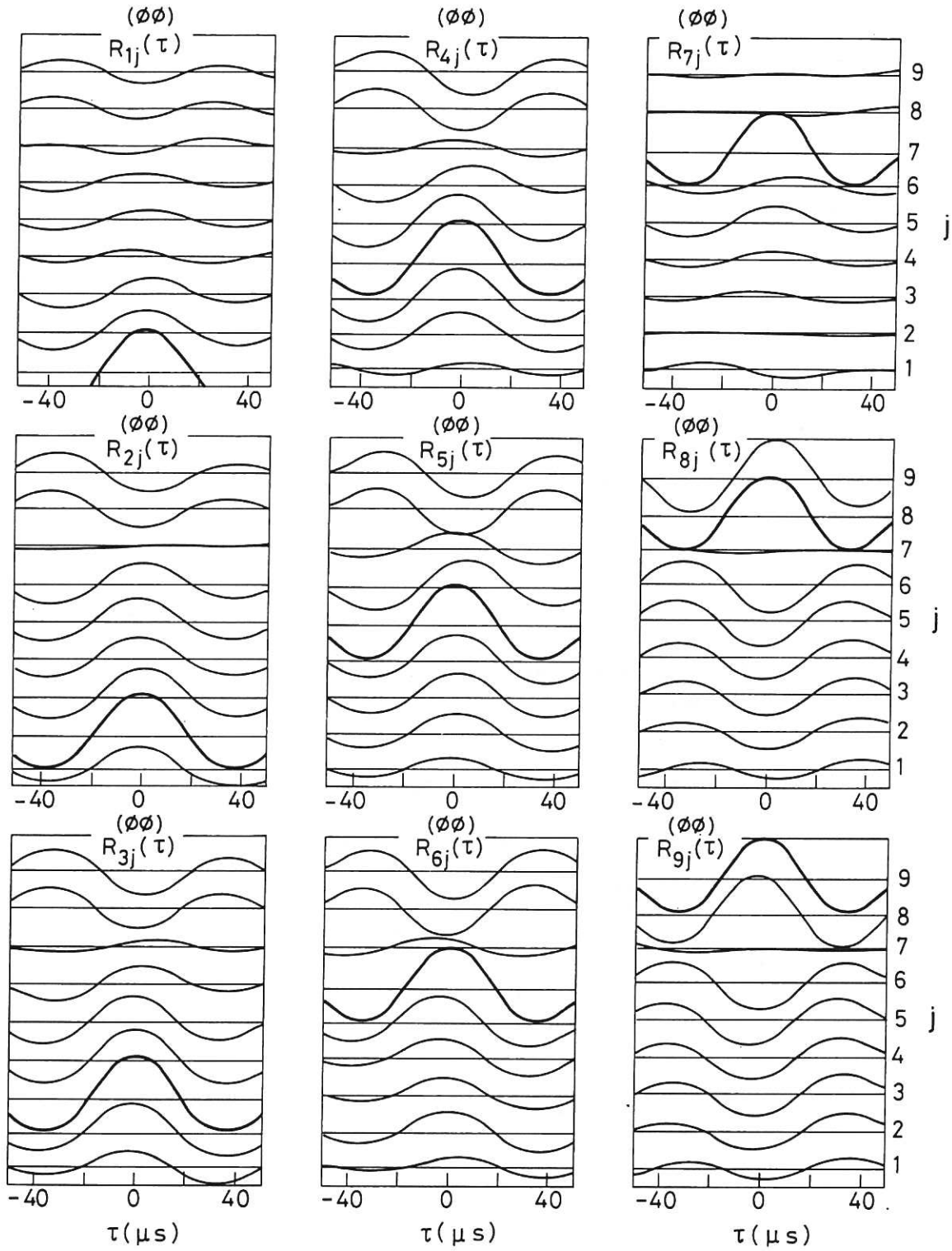


Fig.5 Time-delayed Correlation matrix for B_ϕ probe signals in the sustainment phase (frequency band 4—20kHz) showing that there is no evidence for radial propagation.

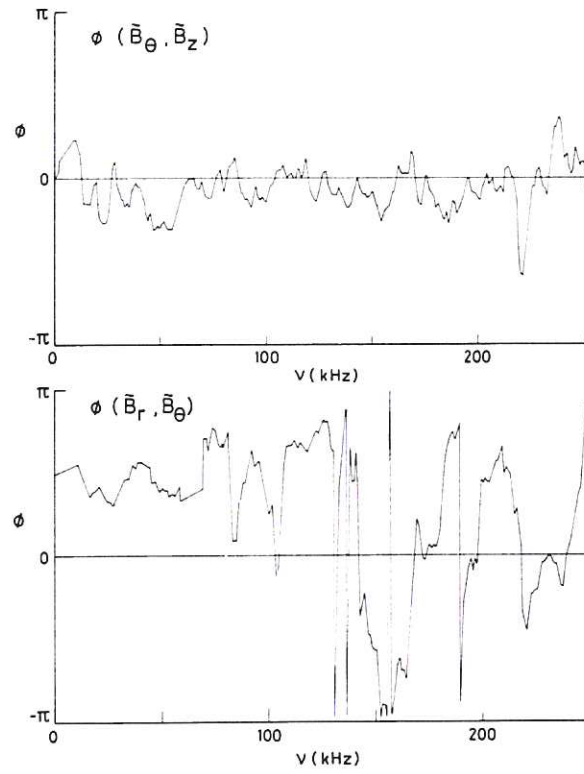


Fig.6 Cross phase spectrum for B_θ , B_ϕ (top) and B_r , B_θ (bottom).

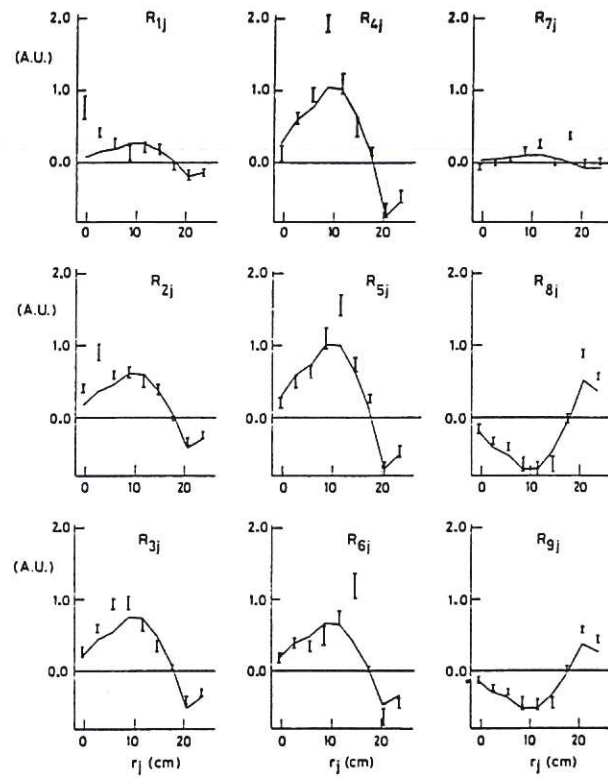


Fig.7 Correlation matrix for B_ϕ (frequency band 4–20kHz) in the sustainment phase and best fit assuming a two-process model.

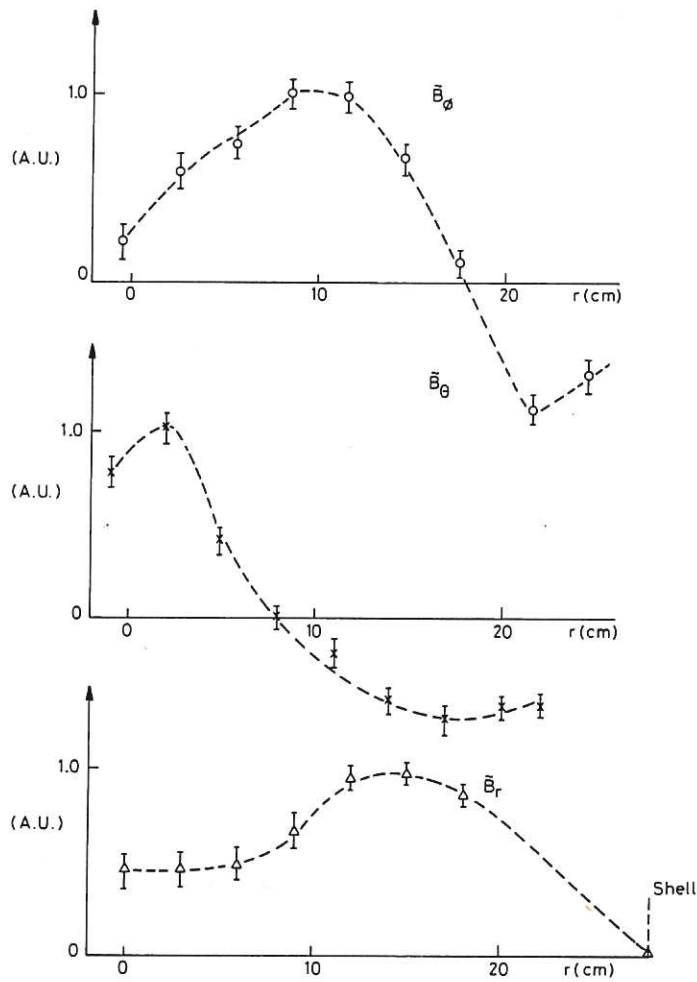


Fig.8 Best fit normalised global radial amplitude distributions for B_ϕ , B_θ , B_r via two-process fit as in Fig.7.

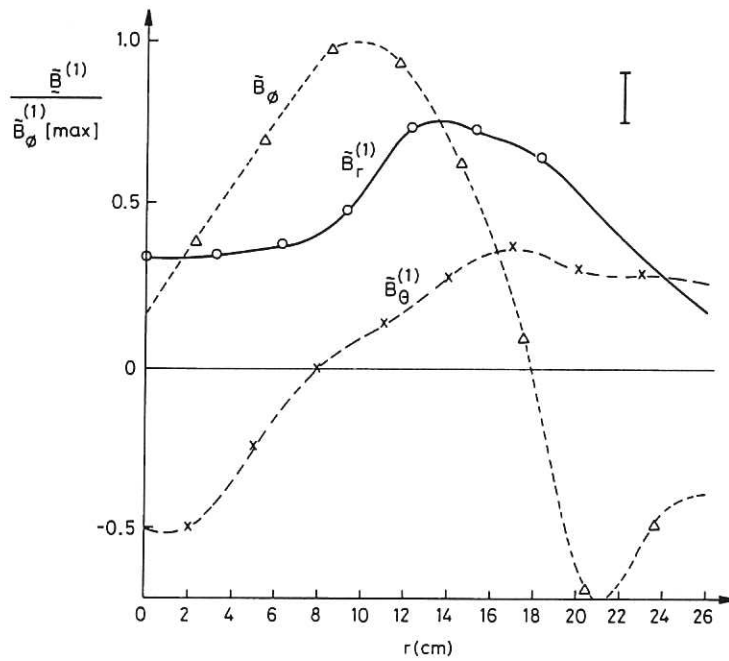


Fig.9 Best fit global radial amplitude vector using 2-process multi-component fit.

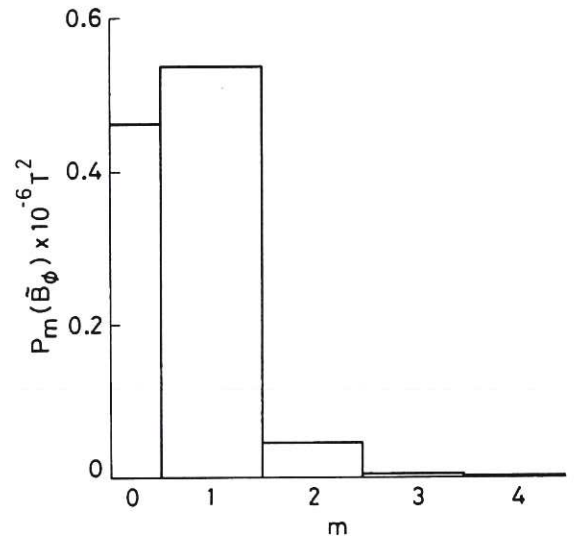
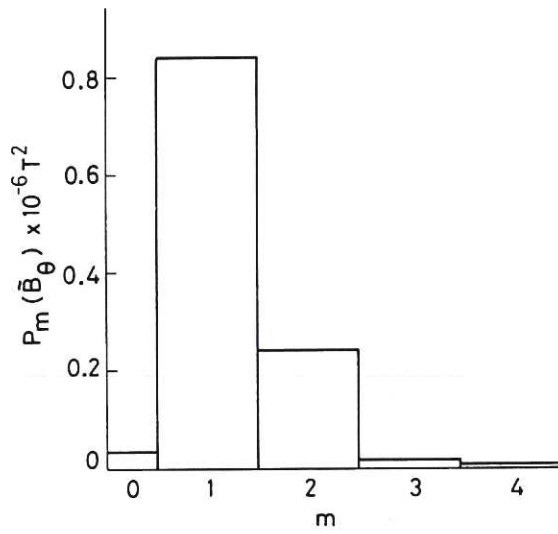
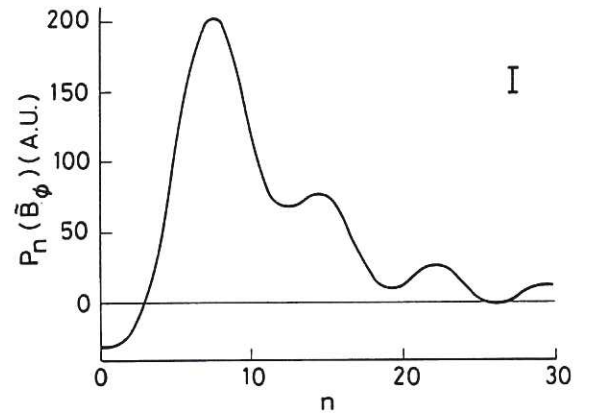
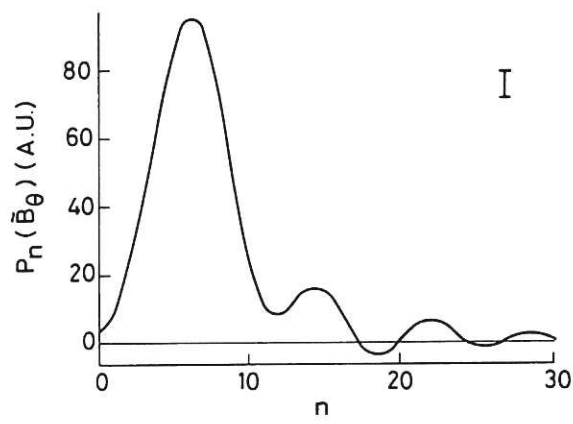


Fig.10 Poloidal and toroidal mode power spectra for B_θ and B_ϕ in the sustainment phase (filter: 4—20kHz).

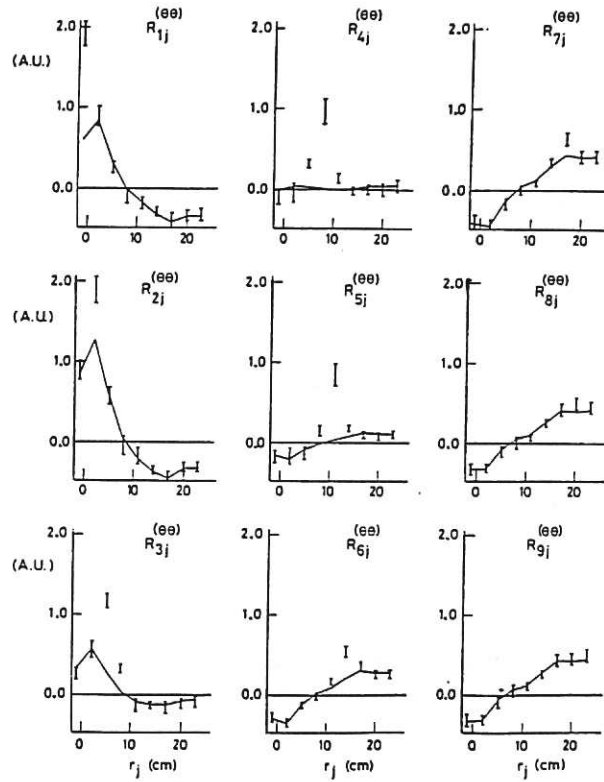


Fig.11 Correlation matrix for B_θ in the sustainment phase (frequency band 4–20kHz) and best fit assuming a 3-process model.

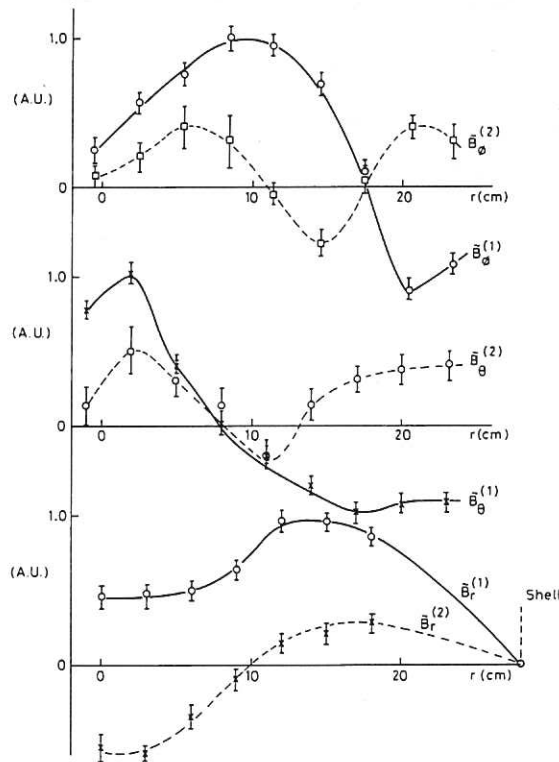


Fig.12 The two global radial amplitude distributions for the fit of Fig.11.

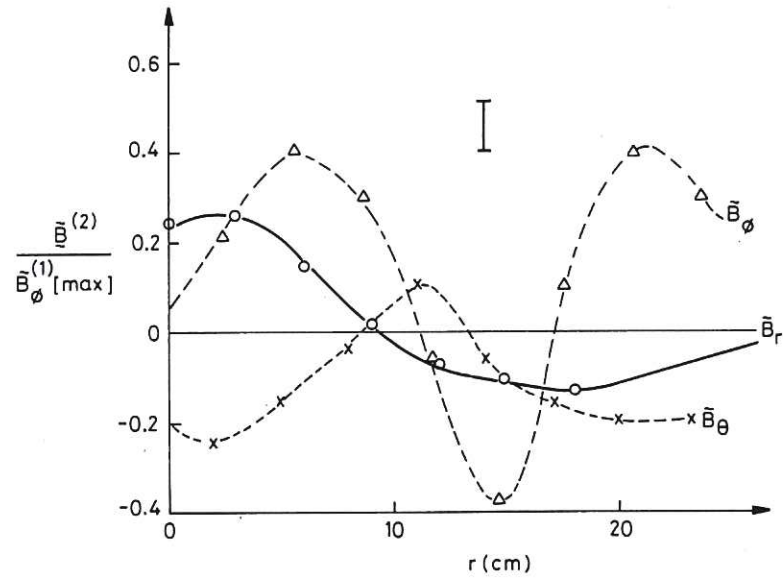


Fig.13 Best fit for the second global radial amplitude vector using a 3-process multi-component fit.

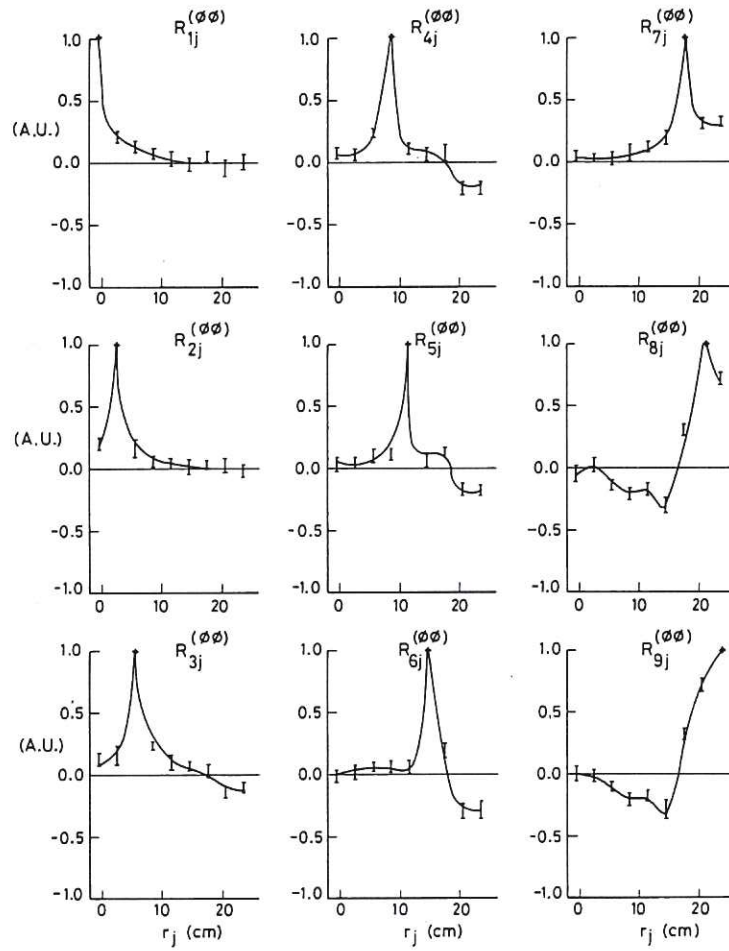


Fig.14 Correlation matrix for B_ϕ in the sustainment phase (frequency band 50–100 kHz).

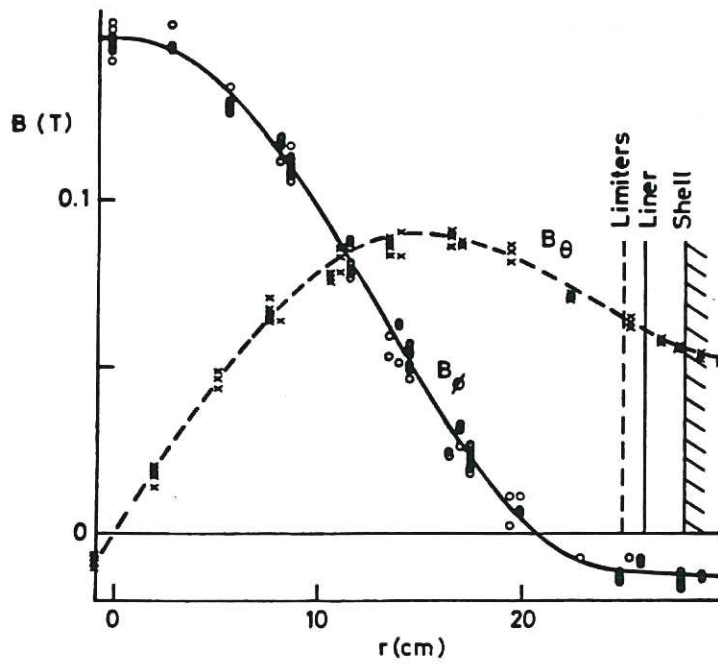


Fig.15 Measured equilibrium field profiles.

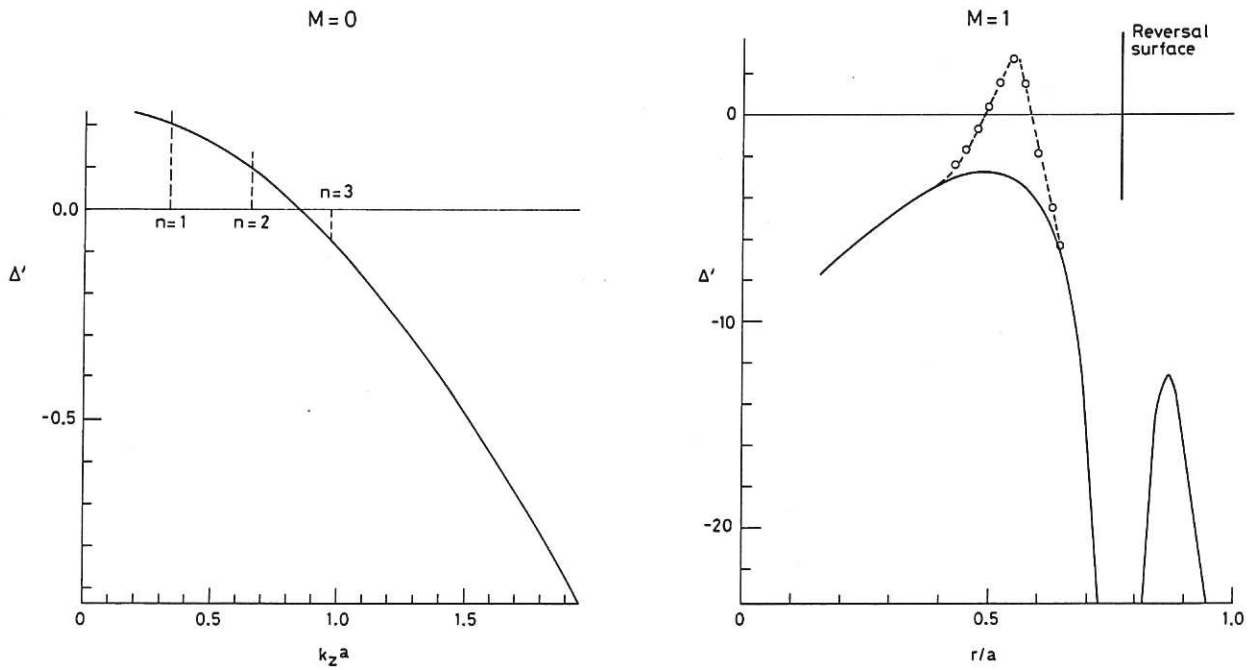


Fig. 16 (a) Δ' as a function of $k_z a$ for $m = 0$ modes using the unperturbed equilibrium of Fig. 17(a).
 (b) Δ' as a function of resonant radius for $m = 1$ modes. Full line refers to the unperturbed equilibrium of Fig. 17(a) and dotted line refers to adjusted equilibrium of Fig. 17(b).

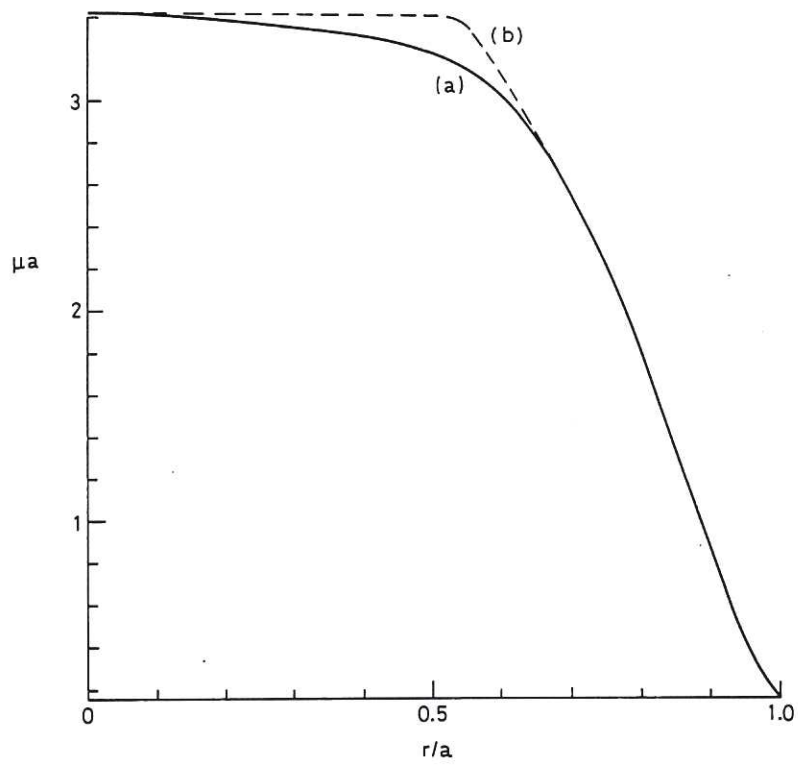


Fig.17(a) Equilibrium μ profile calculated from probe measurements and (b) adjusted μ profile on the limits of experimental error.

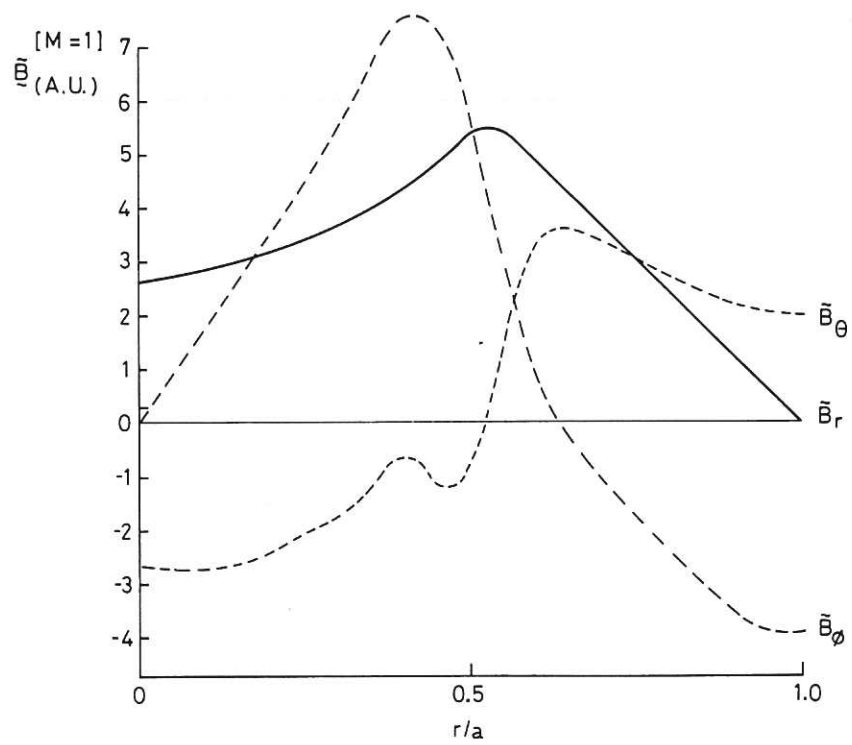


Fig. 18 Calculated linear $m = 1$ eigenfunctions corresponding to the largest value of Δ' in Fig. 16(a).

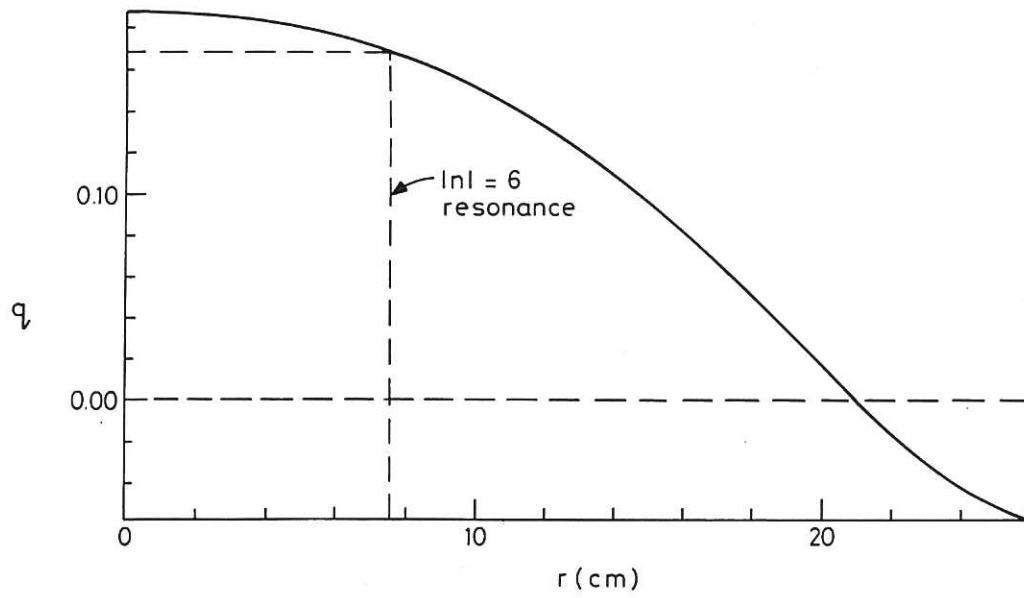


Fig.19 Measured equilibrium q-profile showing the closest integral n number to the axis.

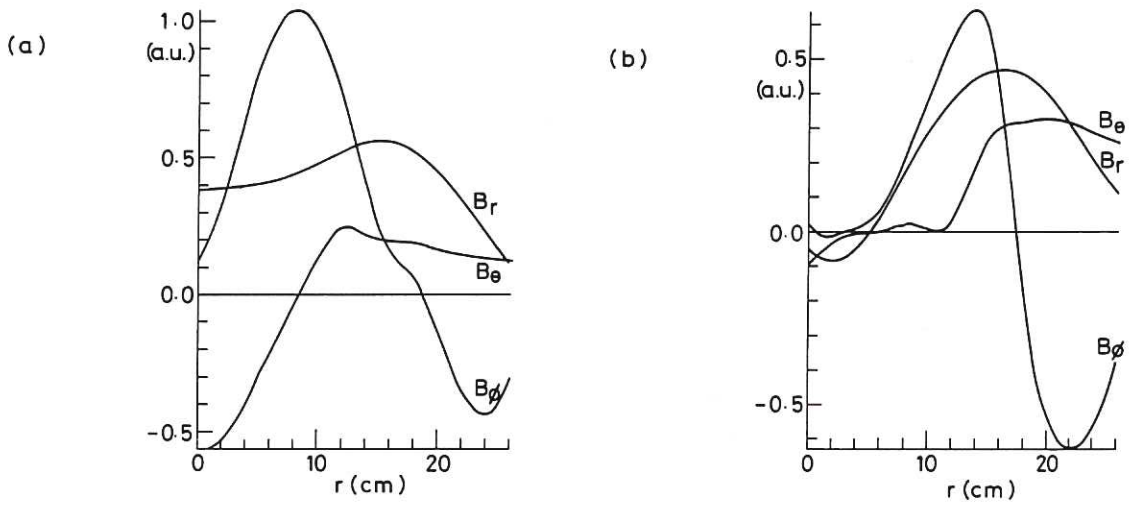


Fig.20 'Rotated' first (a) and second (b) global processes showing

- (i) first process almost unchanged and
- (ii) for second process:

$B_r = B_\theta = B_\phi = 0$ for $r = 0$ to $r = 6$ cm suggesting correspondence with low frequency ideal linear instability.

